RSC Advances

PAPER

View Article Online
View Journal | View Issue

Cite this: *RSC Adv.*, 2020, **10**, 14630

Porous niobia spheres with large surface area: alcothermal synthesis and controlling of their composition and phase transition behaviour†

Yoshitaka Kumabe,[a] Hitomi Taga,[a] Kai Kan,[abc] Masataka Ohtani *[abc] and Kazuya Kobiro *[abc]

Received 22nd February 2020
Accepted 3rd April 2020

DOI: 10.1039/d0ra01704c

rsc.li/rsc-advances

Submicron-sized niobia (Nb_2O_5) porous spheres with a high specific surface area (300 m^2 g^{-1}) and nano concave–convex surfaces were synthesized *via* a rapid one-pot single-step alcothermal reaction. Prolonged reaction time or high reaction temperatures resulted in a morphology change of Nb_2O_5 from amorphous sphere to rod crystals with hexagonal crystal phase. A similar alcothermal reaction yielded TiO_2–Nb_2O_5 composite porous spheres, whose Ti : Nb molar ratio was controlled by changing the precursor solution component ratios. A simple thermal treatment of amorphous TiO_2–Nb_2O_5 porous spheres consisting of 1 : 2 (molar ratio) Ti : Nb at 600 °C for 2 h induced crystal phase transfer from amorphous to a monoclinic crystal phase of submicron-sized $TiNb_2O_7$ porous spheres with a specific surface area of 50 m^2 g^{-1}.

Introduction

Porous materials, including activated carbon, SiO_2, metal oxides, zeolites, and metal–organic frameworks (MOFs), are promising functional materials because of their large surface area that can be used to adsorb several materials and achieve material storage-release for material transfer. These unique properties allow for applications such as gas storage and separation, catalysis, and catalyst supports.[1] In particular, metal oxides are intriguing because of their intrinsic high-temperature stability and durability.[2]

To obtain porous materials, several methods, including solution combustion,[3] dealloying,[4] electrochemical deposition,[5] spray pyrolysis,[6] sol–gel method,[7] as well as hydrothermal and solvothermal methods,[8] have been developed. In particular, the solvothermal method using high-temperature non-aqueous solvents as reaction media is a novel approach to prepare size-, morphology-, and stoichiometry-controlled metal oxides. In this context, a unique one-pot and single-step solvothermal method was developed to afford SiO_2, TiO_2, ZnO, ZrO_2, and CeO_2 with porous spherical morphologies, where numerous few nm-sized primary particles aggregate to yield a spherical secondary morphology with a few hundred nm in diameter.[9] These porous spheres were named meso/macroporously architected roundly integrated metal oxides (MARIMOs). The large surface areas of MARIMOs with micro- and mesopores and nano concave–convex surface structure impart their unique abilities. Both solid and hollow MARIMOs can be obtained with TiO_2. In addition, composite MARIMOs, including CeO_2–ZrO_2,[10] Al_2O_3–TiO_2,[11] ZnO–TiO_2,[11] SiO_2–TiO_2,[12] Co/Mn oxide,[13] Ni/Mn oxide,[13] and Co/Mn/Fe oxide[13] have been prepared *via* the solvothermal method with tightly controllable stoichiometry. Thus, solvothermal method is a versatile approach for obtaining metal oxides with a porous spherical structure, large surface area, and nano concave–convex surface structure.

Nb_2O_5 has been used as a photocatalyst,[14,15] solid acid,[16] catalyst support,[17,18] and anode material for lithium and sodium ion batteries.[19] Several preparation methods are available for these materials.[20] For example, Li *et al.* prepared monodisperse glycolated niobium oxide spheres *via* a simple antisolvent precipitation approach. Mesoporous niobium oxide spheres with a high specific surface area of 312 m^2 g^{-1} were obtained by hydrothermal treatment.[21] Li *et al.* synthesized Nb_2O_5 hollow nanospheres by heating a water solution of niobium oxalate and sodium dihydrogen phosphate dihydrate at 220 °C for 48 h.[22] Dai *et al.* prepared monodispersed Nb_2O_5 microspheres *via* a facile one-pot solvothermal route using an isopropyl alcohol solution of niobium pentachloride and tetrabutyl ammonium hydroxide at 200 °C for 24 h.[23] However, simpler preparation methods should be developed for further acceleration of their practical uses. Thus, niobium oxide and variants of MARIMOs with large surface area were prepared herein using a facile synthesis method for Nb_2O_5, TiO_2–Nb_2O_5 composite, and $TiNb_2O_7$ MARIMOs.

[a]*School of Environmental Science and Engineering, Kochi University of Technology, 185 Miyanokuchi, Tosayamada, Kami, Kochi 782-8502, Japan. E-mail: ohtani.masataka@kochi-tech.ac.jp; kobiro.kazuya@kochi-tech.ac.jp*

[b]*Laboratory for Structural Nanochemistry, Kochi University of Technology, 185 Miyanokuchi, Tosayamada, Kami, Kochi 782-8502, Japan*

[c]*Research Center for Material Science and Engineering, Kochi University of Technology, 185 Miyanokuchi, Tosayamada, Kami, Kochi 782-8502, Japan*

† Electronic supplementary information (ESI) available. See DOI: 10.1039/d0ra01704c

Results & discussion

Synthesis and morphology changes of Nb_2O_5 MARIMO

Nb_2O_5 MARIMO was prepared according to a similar method reported previously (entry 1 in Table 1).[9] Simple heating of a methanol solution of $Nb(OEt)_5$ and formic acid at 300 °C for 10 min afforded Nb_2O_5 MARIMO in high yield (>90%). The scanning electron microscopy (SEM) images revealed that the obtained Nb_2O_5 MARIMO was perfectly monodispersed (Fig. 1a(i)), and their shape was approximately spherical with a diameter of 630 ± 50 nm (Fig. 1a(ii), 1b(i) and S1,† red line). Also, the obtained Nb_2O_5 MARIMO was composed of many amounts of a few nm sized primary particles (Fig. 1b(ii)). The formation mechanism of Nb_2O_5 MARIMO was expected to be similar to a proposed mechanism in our previous report.[9] In the initial steps of the reaction, primitive niobium alkoxide oligomers are formed in high-temperature methanol and interconnected *via* surface interactions with carboxyl groups. As the further heating reaction of precursor mixture proceeds, niobium alkoxide oligomers react with the water, which generated by esterification of formic acid and methanol and/or dehydration condensation of methanol, to form Nb_2O_5. The pore structures are formed by gaseous products, such as CO_2 and hydrocarbons generated by decomposition of alkoxide and formic acid, trapped inside the sphere. The Nb_2O_5 MARIMO obtained without formic acid was polydisperse and obtained in low yield (<40%; Fig. S2a†). In addition, when the solvent was changed to water, spherical shapes were not formed (Fig. S2b†). From the results of the control experiment, the combination of $Nb(OEt)_5$, formic acid, and methanol is essential for the formation of a spherical morphology and high yield.

The direct evidence of the formation of a pore in Nb_2O_5 spheres was confirmed by nitrogen adsorption–desorption measurements (Fig. S3a(i)†). If the obtained Nb_2O_5 MARIMO has no pores, the specific surface area should be a few $m^2\ g^{-1}$ estimated from the diameter (*ca.* 630 nm) and specific density (d = 4.6 g cm^{-3}). Contrary to this expectation, the obtained Nb_2O_5 MARIMO showed a high specific surface area (302 $m^2\ g^{-1}$) and porous structure less than 10 nm-sized (Fig. S3a(ii)†). This fact strongly supports the presence of the penetrated pore inside the spherical particles.

To further characterization of the obtained Nb_2O_5 MARIMO, powder X-ray diffraction (XRD) and electron microscopic measurements were performed. No peaks were observed in the corresponding XRD pattern (Fig. 2c, red line), and no fringe structure in the Nb_2O_5 MARIMO primary particle was observed in the high-resolution transmission electron microscopy (HR-TEM) image (Fig. 1b(ii)). This indicated that the obtained Nb_2O_5 MARIMO was not crystalline but amorphous.

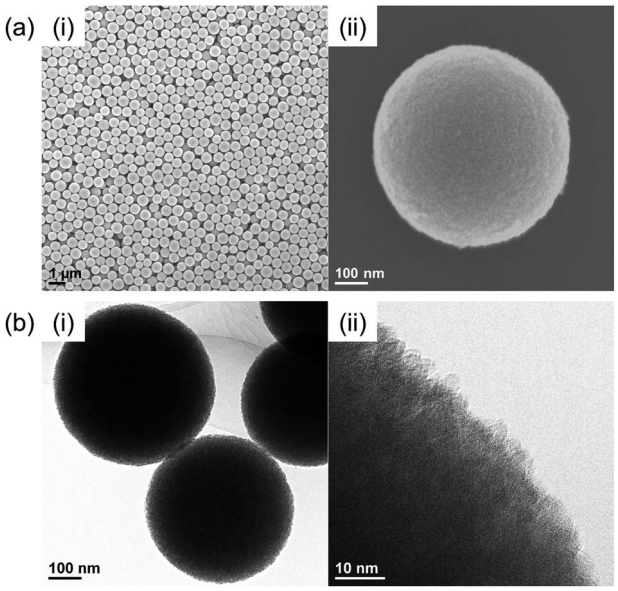

Fig. 1 (a) SEM and (b) TEM images of the prepared Nb_2O_5 MARIMO at (i) low magnification and (ii) high magnification.

To date, almost 15 polymorphic forms of Nb_2O_5 have been reported; however, hexagonal, orthorhombic, and monoclinic phases are relatively common.[20] The crystal phases significantly affect the activity of the photocatalyst[24] and solid acid.[25] Thus, it is important to control of the crystal phase formation in the obtained Nb_2O_5 MARIMO. The easiest method to improve the crystallinity is further heating. When the heating time of the precursor solution was prolonged to 60 min, the crystal phase dramatically changed from amorphous to the hexagonal phase of Nb_2O_5 (Fig. 2c). This was concomitant with a drastic morphology change from spherical to rod-shaped (Fig. 2a(ii)). The corresponding HR-TEM image (Fig. 2b) showed that the crystal lattice distances were 0.39 nm. In addition, the fast Fourier transform (FFT) pattern in the HR-TEM image indicated

Table 1 Molar ratios of Ti and Nb, specific surface area, pore size, and TiO_2 crystalline size of the prepared MARIMOs

Entry	Sample name of MARIMO[a]	Molar ratio of Ti and Nb: Precursor solution	Molar ratio of Ti and Nb: Product[b]	Specific surface area[c] [$m^2\ g^{-1}$]	Pore size[d] [nm]	TiO_2 crystalline size[e] [nm]
1	Nb_2O_5	0 : 100	—	302	3.3	—
2	TiO_2–Nb_2O_5-75	25 : 75	21.7 : 78.3	274	5.9	34.7
3	TiO_2–Nb_2O_5-50	50 : 50	50.1 : 49.9	200	8.9	13.6
4	TiO_2–Nb_2O_5-25	75 : 25	74.3 : 25.7	250	3.4	10.0
5	TiO_2	100 : 0	—	234	3.6	9.6

[a] Denotes the atomic% of Nb to total number of Nb and Ti atoms. [b] Evaluated by STEM/EDX analysis. [c] BET method. [d] BJH plot. [e] Estimated using the Scherrer equation.

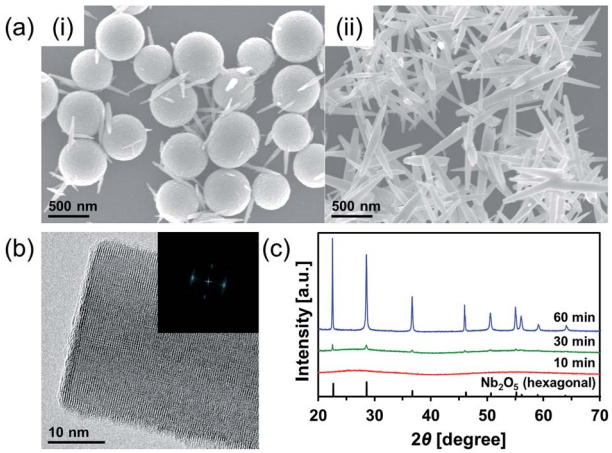

Fig. 2 (a) SEM images of the Nb_2O_5 obtained at 300 °C with different solvothermal-reaction times (i) 30 min and (ii) 60 min. (b) HR-TEM image of the rod-like Nb_2O_5; corresponding FFT image is inset. (c) XRD patterns of the powdery products obtained using different solvothermal-reaction times (blue, 60 min; green, 30 min; red, 10 min). Reference peaks of hexagonal Nb_2O_5 (JCPDS 00-007-0061) are represented by the black line.

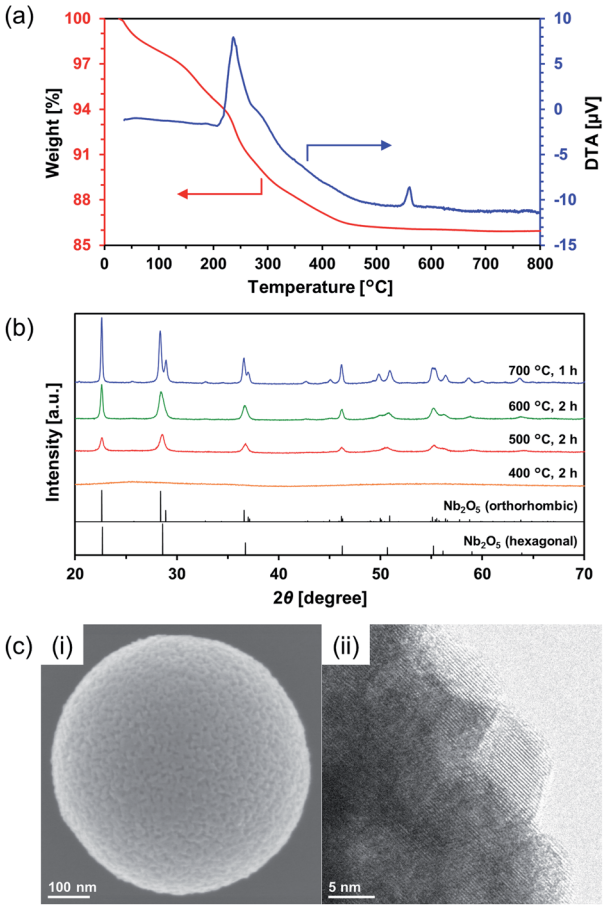

Fig. 3 (a) TG-DTA profiles of the as-synthesized Nb_2O_5 MARIMO measured in air at a heating rate of 2 °C min^{-1}. (b) XRD patterns of calcined Nb_2O_5 MARIMO at 400–700 °C (blue, 700 °C; green, 600 °C; red, 500 °C; orange, 400 °C). Reference peaks of orthorhombic Nb_2O_5 (JCPDS 01-071-0336) and hexagonal Nb_2O_5 (JCPDS 00-007-0061) are represented by black lines. (c) SEM (i) and HR-TEM (ii) images of the Nb_2O_5 MARIMO calcined at 500 °C for 2 h. The crystal lattice distances were 0.31 nm.

that the direction of rod growth was along the [001] facet. When a 30 min heating procedure was used, spheres and rods coexisted. Compared to 10 min heating, a volume reduction of approximately 40% was observed for the 30 min heating process, where the diameter of the obtained Nb_2O_5 MARIMO decreased to 530 ± 50 nm (Fig. 2a(i) and S1,† blue line). Ostwald ripening was likely responsible for this shrinkage.[26,27] Similarly, higher reaction temperatures (325 and 350 °C) with a fixed reaction time (10 min) resulted in rod-like hexagonal phase nanocrystals (Fig. S4†). Although the crystallinity was successfully improved by extending the reaction time or using a high reaction temperature, the porosity was lost due to the morphology change, and the specific surface area was greatly reduced.

Calcination of the as-synthesized amorphous Nb_2O_5 MARIMO was used as an alternative method to change the crystal phase. Generally, amorphous Nb_2O_5 crystallizes at 500 °C into hexagonal or orthorhombic phase, tetragonal phase at 800 °C, and monoclinic phase at >1000 °C.[28] An exothermic phenomenon was observed at approximately 240 and 560 °C in the thermogravimetric-differential thermal analysis (TG-DTA, Fig. 3a). The exothermic peak at approximately 240 °C originated from the combustion of organic residues included in MARIMO. In addition, the exothermic peak with negligible weight loss at approximately 560 °C was assigned to a crystalline phase transfer.[29] Calcination of the as-synthesized amorphous Nb_2O_5 MARIMO yielded a hexagonal phase at 500 °C and an orthorhombic phase at >600 °C, as determined from their XRD patterns (Fig. 3b). The spherical morphology was maintained at ≤600 °C, but collapsed at 700 °C (Fig. 3c(i) and S5†). Thus, Nb_2O_5 MARIMO with improved crystallinity was successfully obtained *via* calcination at 500 or 600 °C for 2 h (Fig. 3b, c and S5a†). The specific surface area of Nb_2O_5 MARIMO calcined at 500 °C was 88 m^2 g^{-1} and average pore size expanded from 3.3 to 6.4 nm upon calcination (Fig. S3b†).

Synthesis of TiO_2–Nb_2O_5 composite MARIMO

Ti–Nb binary oxides have attracted significant attention since their discovery as they exhibit reduced electrical resistance,[30] high photocatalytic activity under visible light irradiation,[31] and controlled Brønsted/Lewis acidity.[32] In particular, using Ti–Nb binary oxides in lithium and sodium ion batteries[19,33,34] has attracted great attention because of its improved electronic conductivity,[35] ion diffusion path expansion,[35] and high theoretical capacity.[36] As mentioned in the introduction, composite MARIMOs consisting of plural metal oxides have been successfully synthesized.[10–13] Herein, a one-pot and single-step technique was used to obtain TiO_2–Nb_2O_5 composite MARIMOs.

A methanol solution of $Ti(O^iPr)_4$ and $Nb(OEt)_5$ with formic acid was heated at 300 °C for 10 min. The molar ratio of Ti to Nb

in the product MARIMO was easily controlled by changing the ratio in the corresponding precursor solution (entries 2–4 in Table 1). Nearly equivalent Ti/Nb ratios between the precursor solutions and products were obtained. As shown in Fig. 4a(i–iii), Ti and Nb atoms were equally distributed at the nano-level in the TiO_2–Nb_2O_5-75, TiO_2–Nb_2O_5-50, and TiO_2–Nb_2O_5-25 samples, where the numbers denote the atomic percentage of Nb among the total number of Nb and Ti atoms. In addition, the TiO_2–Nb_2O_5 composite MARIMOs were highly porous with specific surface areas of >200 $m^2\ g^{-1}$ (Table 1 and Fig. S6†).

Only the tetragonal (anatase-type) TiO_2 peaks were observed in the XRD profiles when Nb atoms were included in the product MARIMOs (Fig. 4b(i)). Lower angle shifts of the diffraction peaks were also observed in the XRD profiles (Fig. 4b(ii)), indicating that the composite MARIMOs consisted of solid solutions and the crystal lattice was enlarged by the doped Nb atoms with larger ionic radii (Nb^{5+} = 0.64 Å, Ti^{4+} = 0.61 Å).[37] Additionally, precursor solutions containing larger amounts of $Nb(OEt)_5$ resulted in the larger primary particle sizes of TiO_2 in the resulting MARIMOs (Table 1). However, this crystalline growth of TiO_2 was not observed for the Al_2O_3–TiO_2, ZnO–TiO_2, and SiO_2–TiO_2 composites.[11,12] Thus, the observed crystalline growth of TiO_2 can be ascribed to the catalytic effect of solid Nb_2O_5 as a solid acid that promoted crystalline growth.

Interestingly, hollow MARIMO were formed at a 50 : 50 Ti/Nb molar ratio (Fig. 4a(ii) and S7†). However, solid TiO_2–Nb_2O_5-50 MARIMO was obtained (Fig. S8†) when the reaction was immediately quenched at 0 min (the reaction temperature was 300 °C). From the XRD patterns, the longer reaction time yielded better crystallinity (Fig. S9†). Ostwald ripening was likely the cause of the hollow MARIMO formation.[38] These unique hollow structures imparted large surface area, low density, and high loading capacity. Therefore, the prepared materials offer promising potential for use in advanced micro-/nanoreactors, catalysis, energy storage/conversion, biomedicine, sensors, and environmental remediation applications.[39–41]

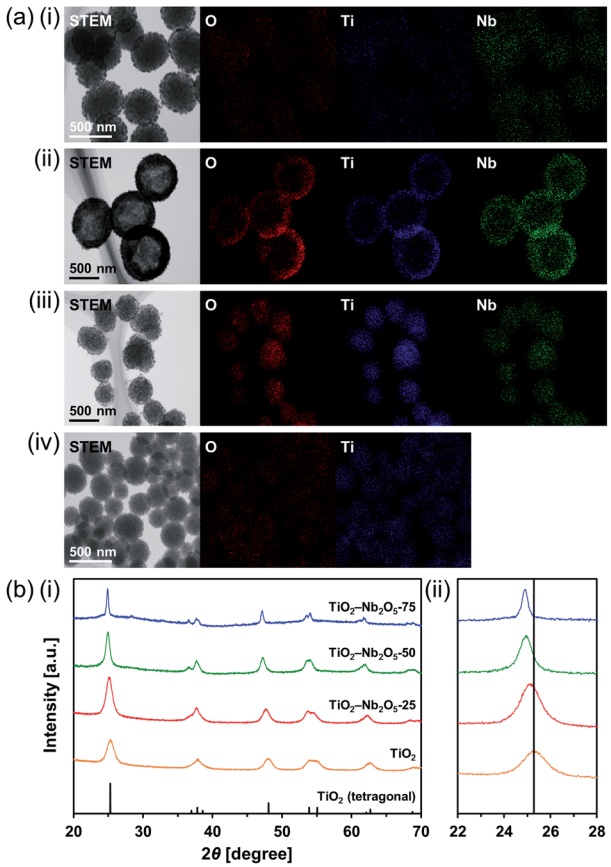

Fig. 4 (a) STEM/EDX analysis of the prepared TiO_2–Nb_2O_5 composite MARIMOs; (i) TiO_2–Nb_2O_5-75, (ii) TiO_2–Nb_2O_5-50, (iii) TiO_2–Nb_2O_5-25, and (iv) TiO_2. (b) XRD patterns of the obtained powdery products prepared with different molar ratios of Ti/Nb (blue, TiO_2–Nb_2O_5-75; green, TiO_2–Nb_2O_5-50; red, TiO_2–Nb_2O_5-25; orange, TiO_2). Reference peaks corresponding to tetragonal TiO_2 (JCPDS 00-021-1272) are represented by the black line. The 2θ range: (i) 20–70°, (ii) 22–28°.

Formation of $TiNb_2O_7$ MARIMO by crystallization of amorphous TiO_2–Nb_2O_5 composite MARIMO

$TiNb_2O_7$ as an anode material for lithium ion batteries has a high theoretical capacity of 387.6 mA h g^{-1} derived from its 5-electron transfer mechanism (Ti^{4+}/Ti^{3+}, Nb^{5+}/Nb^{4+}, and Nb^{4+}/Nb^{3+}). This value is approximately two times higher than that of the commonly used $Li_4Ti_5O_{12}$ (175 mA h g^{-1}).[36] Thus, $TiNb_2O_7$ has attracted significant attention is promising for application in electric vehicles.[19,33,34] However, $TiNb_2O_7$ suffers from low ionic and electric conductivity. Tailoring special nanostructures of $TiNb_2O_7$ can be used to harness the advantages of nanomaterials, including high electrode/electrolyte contact area and short ion diffusion distances. In particular, microscale spherical materials with hierarchical nanoscale structure are promising for solving the drawbacks of pure nanoscale porous materials with low tap densities and poor coulombic efficiency. Although, the syntheses of $TiNb_2O_7$ porous spheres have been previously reported, those with larger surface areas remain elusive (Table S1†). Thus, to obtain $TiNb_2O_7$ porous spheres with large surface area, the synthetic conditions of the precursor composite TiO_2–Nb_2O_5 as well as the calcination conditions were closely examined.

First, a similar alcothermal treatment of a 1 : 2 (mol ratio) $Ti(O^iPr)_4$ and $Nb(OEt)_5$ mixed methanol solution including formic acid at 300 °C afforded a precursor composite MARIMO with tetragonal (anatase-type) TiO_2 and amorphous Nb_2O_5 as determined from its XRD pattern (Fig. S10,† blue line). The corresponding SEM images revealed characteristically large primary particles on the MARIMO surface (Fig. S11a(i)†). The second step involved calcination of the precursor MARIMO at 700 °C for 2 h and yielded monoclinic $TiNb_2O_7$ MARIMO (Fig. S11a(ii) and S12a†, blue line). However, the XRD patterns showed that the calcined MARIMO contained mainly monoclinic $TiNb_2O_7$ with a small amount of tetragonal (anatase-type) TiO_2 and orthorhombic Nb_2O_5 (Fig. S12b†, blue line). This indicates that a pure $TiNb_2O_7$ MARIMO was not afforded by the calcination of the as-synthesized TiO_2–Nb_2O_5 MARIMO obtained at 300 °C.

Therefore, amorphous TiO_2–Nb_2O_5 composite MARIMO was selected as an alternative precursor (Fig. S10, red line and

S11b(i)†). The material was prepared using a lower temperature (200 °C) alcothermal reaction. As shown in Fig. 5a, calcination of the amorphous TiO_2–Nb_2O_5 composite MARIMO at >600 °C for 2 h produced the desired $TiNb_2O_7$ MARIMO with a pure monoclinic phase. In addition, tetragonal (anatase-type) TiO_2 and orthorhombic Nb_2O_5 peaks were not observed even in case of the obtained sample at 700 °C (Fig. S12b†, red line). Fringe structures were observed in the HR-TEM image (Fig. 5b(i)) of the primary particles, clearly showing that the MARIMO was composed of single crystals of $TiNb_2O_7$. The $TiNb_2O_7$ porous morphology was clearly demonstrated by high angle annular dark-field scanning transmission electron microscopy (HAADF-STEM; Fig. 5b(ii)). The specific surface area of the obtained monoclinic $TiNb_2O_7$ MARIMO was smaller (50 $m^2 g^{-1}$) than that before calcination (Fig. S13†, 497 $m^2 g^{-1}$), but 50 $m^2 g^{-1}$ is the highest value reported for this type of material to the best of our knowledge (Fig. 5c(i) and Table S1†). As expected, the average pore size was enlarged from 2.5 to 8.8 nm (Fig. 5c(ii)), which is favourable for guest materials to access deep into the porous spheres. In addition, the pore space between the $TiNb_2O_7$ MARIMO can buffer volume changes derived from the phase transitions occurring during lithiation/delithiation, which may result in good cycling performance *via* enhanced structural stability.[42] Thus, $TiNb_2O_7$ porous spheres were successfully prepared with a monoclinic crystal phase and wide pores by calcination of the amorphous TiO_2–Nb_2O_5 composite MARIMO precursor.

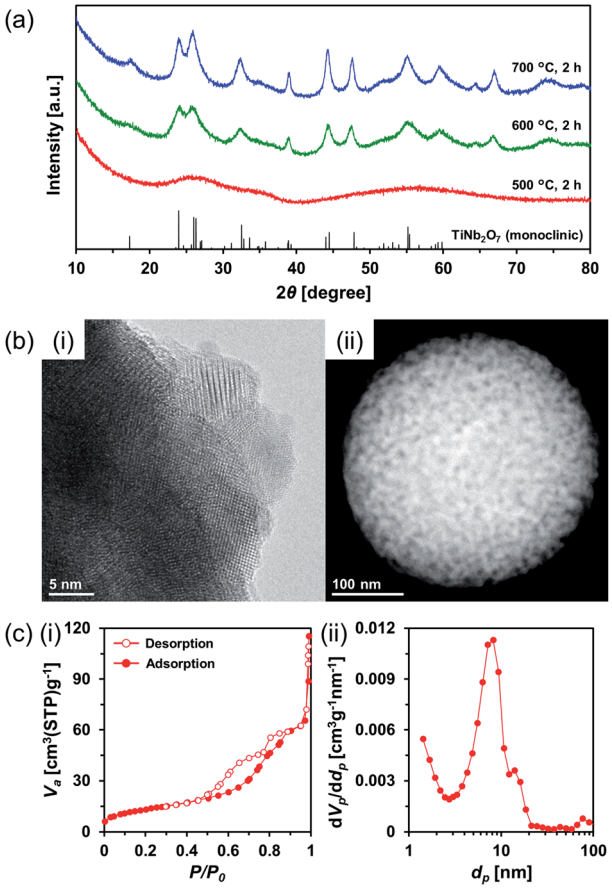

Fig. 5 (a) XRD patterns of the calcined amorphous TiO_2–Nb_2O_5 composite MARIMO at 500–700 °C (blue, 700 °C; green, 600 °C; red, 500 °C). Reference peaks of monoclinic $TiNb_2O_7$ (JCPDS 00-039-1407) are indicated by the black line. (b) HR-TEM (i) and HAADF-STEM (ii) images of the amorphous TiO_2–Nb_2O_5 composite MARIMO calcined at 600 °C. (c) Nitrogen adsorption–desorption isotherms (i) and pore size distributions (ii) of the amorphous TiO_2–Nb_2O_5 composite MARIMO calcined at 600 °C.

Conclusions

Monodispersed Nb_2O_5 porous spheres (Nb_2O_5 MARIMO) with 630 nm in diameter were prepared *via* the simple alcothermal reaction of a methanol solution of $Nb(OEt)_5$ with formic acid. The crystallinity and pore size of the prepared Nb_2O_5 MARIMO were improved by prolonging the reaction time or simple calcination of the product. TiO_2–Nb_2O_5 composite MARIMO was obtained using a similar alcothermal reaction of $Ti(O^iPr)_4$, $Nb(OEt)_5$, and formic acid in methanol, with a product Ti : Nb atomic ratio that was controlled by changing molar ratio of $Ti(O^iPr)_4$ and $Nb(OEt)_5$ in the precursor solution. A two-step synthetic approach for the generation of $TiNb_2O_7$ porous spheres was developed *via* an alcothermal treatment of a 1 : 2 (molar ratio) mixed solution of $Ti(O^iPr)_4$ and $Nb(OEt)_5$ in methanol followed by simple calcination. Considering the fact that the obtained submicron-sized porous spheres of niobia and their composites have a large surface area, high performance can be expected in the field of catalysts and batteries. To evaluate catalyst and battery performance, the research for a practical application is undergoing.

Experimental section

Materials

Methanol, formic acid, niobium(v) ethoxide [$Nb(OEt)_5$], and titanium tetraisopropoxide [$Ti(O^iPr)_4$] were obtained from FUJIFILM Wako Pure Chemical Corporation. All reagents were used as received unless otherwise noted.

Synthetic procedure

Synthesis of Nb_2O_5 MARIMO. First, $Nb(OEt)_5$ (0.35 mmol) was added to a solution of formic acid (1.75 mmol) in methanol (3.5 mL) under vigorous stirring. The resultant precursor solution was transferred to an SUS-316 stainless steel tubular reactor with a 10 mL inner volume and the reactor was then sealed with an SUS-316 screw cap. The sealed reactor was heated to 300 °C at a rate of 5.4 °C min^{-1} and the temperature was maintained at 300 °C for 10 min. The reaction was quenched by placing the reactor in an ice-water bath. The obtained precipitates were centrifuged, washed several times with methanol, and dried under vacuum to afford a powdery product.

Synthesis of TiO_2–Nb_2O_5 composite MARIMOs. Aliquots of $Ti(O^iPr)_4$ and $Nb(OEt)_5$ were added to a solution of formic acid (1.75 mmol) in methanol (3.5 mL) under vigorous stirring. Similar treatments of the solution as the above mentioned

Nb_2O_5 MARIMO synthesis yielded the TiO_2–Nb_2O_5 composite MARIMO powdery products.

Formation of $TiNb_2O_7$ MARIMO *via* crystallization of the amorphous TiO_2–Nb_2O_5 composite MARIMO. First, $Ti(O^iPr)_4$ (0.58 mmol) and $Nb(OEt)_5$ (1.17 mmol) was added to a solution of formic acid (8.75 mmol) in methanol (17.5 mL) under vigorous stirring. The resultant precursor solution was sealed in a Teflon-lined autoclave with a 50 mL inner volume. The sealed autoclave was heated to 200 °C at a rate of 5.4 °C min^{-1} and the temperature was maintained at 200 °C for 3 h. After cooling at room temperature, the precipitates were centrifuged, washed several times with methanol, and dried under vacuum to afford a powdery amorphous TiO_2–Nb_2O_5 composite MARIMO. The obtained product was calcined in air at 600 °C for 2 h at 2 °C min^{-1} heating rate to yield the final product.

Characterization methods

Transmission electron microscopy. The transmission electron microscopy (TEM) images were obtained using a JEOL JEM-2100F microscope. The specimens were prepared as follows: samples were dispersed in methanol; 10 μL of the resultant dispersion was drop-casted onto a carbon-coated copper micro grid (Okenshoji, Japan); and the solvent was evaporated under atmospheric pressure. Energy-dispersive X-ray (EDX) mapping and line-scan plots for the STEM images were obtained using an Oxford INCA X-max 80 EDX spectrometer.

Scanning electron microscopy. Scanning electron microscopy (SEM) was performed using a Hitachi SU8020 FE-SEM microscope. The specimens were prepared by drop-casting the sample dispersion on a silicon wafer.

X-ray diffraction measurements. X-ray diffraction (XRD) patterns were recorded using a Rigaku SmartLab diffractometer with graphite-monochromatized Cu Kα radiation (X-ray wavelength: 1.5418 Å) in steps of 0.02° over the 2θ range of 10–80°. The powdery samples were placed on a non-refractive silicon holder (Overseas X-ray Service, Japan). The average TiO_2 crystalline sizes were estimated from the obtained (101) peaks using the Scherrer equation.

Thermogravimetric-differential thermal analysis. Thermogravimetric-differential thermal analysis (TG-DTA) was performed using a HITACHI STA7200RV instrument. The samples were placed on an open platinum sample pan and the experiments were conducted in air at a 2 °C min^{-1} heating rate.

Nitrogen adsorption–desorption isotherm measurements. Nitrogen adsorption–desorption isotherms were obtained using a Belsorp Mini II instrument (MicrotracBEL Corp.). The specific surface areas were determined using the Brunauer–Emmett–Teller (BET) multipoint method with BELMaster7 software. The average pore size distributions were calculated using the Barrette–Joyner–Halenda (BJH) method from the nitrogen adsorption isotherm data.

Conflicts of interest

There are no conflicts to declare.

Acknowledgements

We acknowledge the financial support of the Creation of New Business and Industry Program through the Kochi Prefectural Industry-Academia-Government Collaboration Research Promotion Operation and funding from JSPS KAKENHI Grant Number 15K06560, 17K14858, and 19K05143. The authors also wish to thank the Research Center for Nanotechnology in Kochi University of Technology for performing TEM and SEM analyses.

References

1 V. Valtchev and L. Tosheva, *Chem. Rev.*, 2013, **113**, 6734–6760.
2 Y. Boyjoo, M. Wang, V. K. Pareek, J. Liu and M. Jaroniec, *Chem. Soc. Rev.*, 2016, **45**, 6013–6047.
3 A. Varma, A. Mukasyan, A. Rogachev and K. V. Manukyan, *Chem. Rev.*, 2016, **116**, 14493–14586.
4 H.-J. Qiu, L. Peng, X. Li, H. T. Xu and Y. Wang, *Corros. Sci.*, 2015, **92**, 16–31.
5 A. Lahiri and F. Endres, *J. Electrochem. Soc.*, 2017, **164**, 597–612.
6 J. Leng, Z. Wang, J. Wang, H.-H. Wu, G. Yan, X. Li, H. Guo, Y. Liu, Q. Zhang and Z. Guo, *Chem. Soc. Rev.*, 2019, **48**, 3015–3072.
7 A. E. Danks, S. R. Hall and Z. Schnepp, *Mater. Horiz.*, 2016, **3**, 91–112.
8 M. K. M. Lane and J. B. Zimmerman, *Green Chem.*, 2019, **21**, 3769–3781.
9 P. Wang, K. Ueno, H. Takigawa and K. Kobiro, *J. Supercrit. Fluids*, 2013, **78**, 124–131.
10 E. K. C. Pradeep, T. Habu, H. Tooriyama, M. Ohtani and K. Kobiro, *J. Supercrit. Fluids*, 2015, **97**, 217–223.
11 E. K. C. Pradeep, M. Ohtani and K. Kobiro, *Eur. J. Inorg. Chem.*, 2015, 5621–5627.
12 H. T. T. Nguyen, T. Habu, M. Ohtani and K. Kobiro, *Eur. J. Inorg. Chem.*, 2017, 3017–3023.
13 M. Ohtani, T. Muraoka, Y. Okimoto and K. Kobiro, *Inorg. Chem.*, 2017, **56**, 11546–11551.
14 S. Furukawa, Y. Ohno, T. Shishido, K. Teramura and T. Tanaka, *ACS Catal.*, 2011, **1**, 1150–1153.
15 H. Liu, N. Gao, M. Y. Liao and X. S. Fang, *Sci. Rep.*, 2015, **5**, 7716.
16 S. M. A. H. Siddiki, M. N. Rashed, M. A. Ali, T. Toyao, P. Hirunsit, M. Ehara and K. Shimizu, *ChemCatChem*, 2018, **10**, 1–15.
17 T. Komanoya, T. Kinemura, Y. Kita, K. Kamata and M. Hara, *J. Am. Chem. Soc.*, 2017, **139**, 11493–11499.
18 E. S. Gnanakumar, N. Chandran, I. V. Kozhevnikov, A. Grau-Atienza, E. V. R. Fernandez, A. Sepulveda-Escribano and N. R. Shiju, *Chem. Eng. Sci.*, 2019, **194**, 2–9.
19 Q. Deng, Y. Fu, C. Zhu and Y. Yu, *Small*, 2019, **15**, 1804884.
20 R. A. Rani, A. S. Zoolfakar, A. P. O'Mullane, M. W. Austin and K. K. Zadeh, *J. Mater. Chem. A*, 2014, **2**, 15683–15703.
21 C. C. Li, J. Dou, L. W. Chen, J. Y. Lin and H. C. Zeng, *ChemCatChem*, 2012, **4**, 1675–1682.

22 L. Li, J. Deng, R. Yu, J. Chen, Z. Wang and X. Xing, *J. Mater. Chem. A*, 2013, **1**, 11894–11900.
23 Z. F. Dai, H. Dai, Y. Zhou, D. L. Liu, G. T. Duan, W. P. Cai and Y. Li, *Adv. Mater. Interfaces*, 2015, **2**, 1500167.
24 H. Zhang, Q. Wu, C. Guo, Y. Wu and T. Wu, *ACS Sustainable Chem. Eng.*, 2017, **5**, 3517–3523.
25 K. Nakajima, J. Hirata, M. Kim, N. K. Gupta, T. Murayama, A. Yoshida, N. Hiyoshi, A. Fukuoka and W. Ueda, *ACS Catal.*, 2018, **8**, 283–290.
26 J. Xue, R. Wang, Z. Zhang and S. Qiu, *Dalton Trans.*, 2016, **45**, 16519–16525.
27 J. Chen, H. Wang, G. Huang, Z. Zhang, L. Han, W. Song, M. Li and Y. Zhang, *J. Alloys Compd.*, 2017, **728**, 19–28.
28 E. I. Ko and J. G. Weissman, *Catal. Today*, 1990, **8**, 27–36.
29 H. Kominami, K. Oki, M. Kohno, S. Onoue, Y. Kera and B. Ohtani, *J. Mater. Chem.*, 2001, **11**, 604–609.
30 G. Li, X. Zhang, H. Lu, C. Tan, K. Chen, H. Lu, J. Gao, Z. Yang, G. Zhu, G. Wang and Z. He, *Sens. Actuators, B*, 2019, **283**, 602–612.
31 L. Kong, C. Wang, H. Zheng, X. Zhang and Y. Liu, *J. Phys. Chem. C*, 2015, **119**, 16623–16632.
32 M. Akizuki and Y. Oshima, *J. Supercrit. Fluids*, 2018, **141**, 173–181.
33 S. Lou, Y. Zhao, J. Wang, G. Yin, C. Du and X. Sun, *Small*, 2019, **15**, 1904740.
34 J. Ma, X. Guo, H. Xue, K. Pan, C. Liu and H. T. Pang, *Chem. Eng. J.*, 2020, **380**, 122428.
35 H. Usui, S. Yoshioka, K. Wasada, M. Shimizu and H. Sakaguchi, *ACS Appl. Mater. Interfaces*, 2015, **7**, 6567–6573.
36 J.-T. Han, Y.-H. Huang and J. B. Goodenough, *Chem. Mater.*, 2011, **23**, 2027–2029.
37 Y. Lv, B. Cai, Q. Ma, Z. Wang, J. Liu and W.-H. Zhang, *RSC Adv.*, 2018, **8**, 20982–20989.
38 H. G. Yang and H. C. Zeng, *J. Phys. Chem. B*, 2004, **108**, 3492–3495.
39 X. Wang, J. Feng, Y. Bai, Q. Zhang and Y. Yin, *Chem. Rev.*, 2016, **116**, 10983–11060.
40 G. Prieto, H. Tüysüz, N. Duyckaerts, J. Knossalla, G.-H. Wang and F. Schüth, *Chem. Rev.*, 2016, **116**, 14056–14119.
41 L. Yu, H. Hu, H. B. Wu and X. W. Lou, *Adv. Mater.*, 2017, **29**, 1604563.
42 G. Liu, L. Zhao, R. Sun, W. Chen, M. Hu, M. Liu, X. Duan and T. Zhang, *Electrochim. Acta*, 2018, **259**, 20–27.

